



Defect properties of InGaAsN layers grown as sub-monolayer digital alloys by molecular beam epitaxy

Artem Baranov, Alexander Gudovskikh, Dmitry Kudryashov, Alexandra Lazarenko, Ivan Morozov, Alexey Mozharov, Ekaterina Nikitina, Evgeny Pirogov, Maxim Sobolev, Kirill Zelentsov, et al.

► To cite this version:

Artem Baranov, Alexander Gudovskikh, Dmitry Kudryashov, Alexandra Lazarenko, Ivan Morozov, et al.. Defect properties of InGaAsN layers grown as sub-monolayer digital alloys by molecular beam epitaxy. *Journal of Applied Physics*, 2018, SPECIAL TOPIC: DEFECTS IN SEMICONDUCTORS 123 (16), pp.161418 - 161418. 10.1063/1.5011371 . hal-01739252

HAL Id: hal-01739252

<https://hal.science/hal-01739252>

Submitted on 11 Jul 2018

HAL is a multi-disciplinary open access archive for the deposit and dissemination of scientific research documents, whether they are published or not. The documents may come from teaching and research institutions in France or abroad, or from public or private research centers.

L'archive ouverte pluridisciplinaire **HAL**, est destinée au dépôt et à la diffusion de documents scientifiques de niveau recherche, publiés ou non, émanant des établissements d'enseignement et de recherche français ou étrangers, des laboratoires publics ou privés.

Defect properties of InGaAsN layers grown as sub-monolayer digital alloys by molecular beam epitaxy

Artem I. Baranov, Alexander S. Gudovskikh, Dmitry A. Kudryashov, Alexandra A. Lazarenko, Ivan A. Morozov, Alexey M. Mozharov, Ekaterina V. Nikitina, Evgeny V. Pirogov, Maxim S. Sobolev, Kirill S. Zelentsov, Anton Yu. Egorov, Arouna Darga, Sylvain Le Gall, and Jean-Paul Kleider

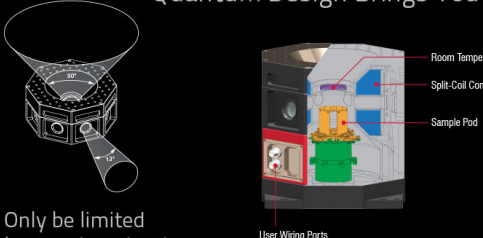
Citation: *Journal of Applied Physics* **123**, 161418 (2018); doi: 10.1063/1.5011371

View online: <https://doi.org/10.1063/1.5011371>

View Table of Contents: <http://aip.scitation.org/toc/jap/123/16>

Published by the *American Institute of Physics*

Quantum Design Brings You the Next Generation Magneto-Optic Cryostat




Only be limited by your imagination...

Learn More

Quantum Design
qdusa.com/opticool5

8 Optical Access Ports: 7 Side; 1 Top
Temperature Range: 1.7 K to 350 K
7 T Split-Coil Conical Magnet
Low Vibration: <10 nm peak-to-peak
89 mm x 84 mm Sample Volume
Automated Temperature & Magnet Control
Cryogen Free



Defect properties of InGaAsN layers grown as sub-monolayer digital alloys by molecular beam epitaxy

Artem I. Baranov,^{1,2,a)} Alexander S. Gudovskikh,¹ Dmitry A. Kudryashov,¹ Alexandra A. Lazarenko,¹ Ivan A. Morozov,¹ Alexey M. Mozharov,¹ Ekaterina V. Nikitina,^{1,3} Evgeny V. Pirogov,¹ Maxim S. Sobolev,¹ Kirill S. Zelentsov,¹ Anton Yu. Egorov,⁴ Arouna Darga,² Sylvain Le Gall,² and Jean-Paul Kleider²

¹Saint-Petersburg National Research Academic University RAS, 194021 Saint-Petersburg, Russia

²GeePs, Group of Electrical Engineering - Paris, UMR 8507 CNRS, CentraleSupélec, Univ. Paris-Sud, Université Paris-Saclay, Sorbonne Universités, UPMC Univ Paris 06, 91192 Gif-sur-Yvette Cedex, France

³Saint-Petersburg Scientific Center RAS, 199034 Saint-Petersburg, Russia

⁴ITMO University, 197101 Saint-Petersburg, Russia

(Received 31 October 2017; accepted 11 February 2018; published online 20 March 2018)

The defect properties of InGaAsN dilute nitrides grown as sub-monolayer digital alloys (SDAs) by molecular beam epitaxy for photovoltaic application were studied by space charge capacitance spectroscopy. Alloys of i-InGaAsN ($E_g = 1.03$ eV) were lattice-matched grown on GaAs wafers as a superlattice of InAs/GaAsN with one monolayer of InAs (<0.5 nm) between wide GaAsN (7–12 nm) layers as active layers in single-junction solar cells. Low p-type background doping was demonstrated at room temperature in samples with InGaAsN layers 900 nm and 1200 nm thick (less $1 \times 10^{15} \text{ cm}^{-3}$). According to admittance spectroscopy and deep-level transient spectroscopy measurements, the SDA approach leads to defect-free growth up to a thickness of 900 nm. An increase in thickness to 1200 nm leads to the formation of non-radiative recombination centers with an activation energy of 0.5 eV ($N_T = 8.4 \times 10^{14} \text{ cm}^{-3}$) and a shallow defect level at 0.20 eV. The last one leads to the appearance of additional doping, but its concentration is low ($N_T = 5 \times 10^{14} \text{ cm}^{-3}$) so it does not affect the photoelectric properties. However, further increase in thickness to 1600 nm, leads to significant growth of its concentration to $(3\text{--}5) \times 10^{15} \text{ cm}^{-3}$, while the concentration of deep levels becomes $1.3 \times 10^{15} \text{ cm}^{-3}$. Therefore, additional free charge carriers appearing due to ionization of the shallow level change the band diagram from p-i-n to p-n junction at room temperature. It leads to a drop of the external quantum efficiency due to the effect of pulling electric field decrease in the p-n junction and an increased number of non-radiative recombination centers that negatively impact lifetimes in InGaAsN. *Published by AIP Publishing.*

<https://doi.org/10.1063/1.5011371>

I. INTRODUCTION

III-V compounds are very attractive in several applications, one of the most important being solar cells (SCs). Indeed, nowadays, multi-junction solar cells (MJSCs) based on III-V compounds have the highest efficiency and have almost reached the psychological barrier of 50% for concentrator photovoltaics.¹ The record values are obtained for bonded² and inverted³ MJSC based on GaInP and GaAs compounds. However, these methods are complicated to transfer to industry so monolithic⁴ MJSCs are still of great interest. Initially, p-n junctions in germanium (0.67 eV) wafers were used for the growth of monolithic triple-junction SCs in combination with GaInP(1.85 eV)/GaAs(1.42 eV).⁵ According to simulations substituting the germanium subcell with a subcell with $E_g = 1$ eV could increase the triple-junction SC efficiency by a few percent, and adding such a subcell to a classical triple-junction would allow one to reach 52% under concentrator illumination.^{6,7} Addition of a small nitrogen content, leads to a reduction of the bandgap of GaAsN ternary alloys by hundreds

of meV.⁸ Additional content of indium allows one to grow $\text{Ga}_{1-x}\text{In}_x\text{N}_y\text{As}_{1-y}$ with $E_g = 1$ eV lattice-matched to GaAs. Though promising results were achieved using InGaAsNSb layers^{9–12} in the last years, MJSC performance is limited by the low lifetime of charge carriers in dilute nitrides.¹³ It is explained by the defect formation due to the low growth temperature, nitrogen incorporation, and unintentional incorporation of different atoms (for example, carbon and hydrogen in vapor phase epitaxy¹⁴). Therefore, equipment of molecular beam epitaxy (MBE) with a RF-plasma nitrogen source is more preferable for the growth of InGaAsN. However, even when grown by MBE, InGaAsN layers have high concentrations of background doping, up to $1 \times 10^{17} \text{ cm}^{-3}$,¹⁵ and of non-radiative recombination centers. Post-growth annealing improves the quality of InGaAsN dilute nitrides.^{16–18} Also, antimony addition inhibits the defect formation and reduces the background doping concentration.^{19–22} However, according to the technological experience of previous growth processes, antimony (Sb) can accumulate on the chamber surface leading to undesirable background doping of layers in top subcells.

In the present work, the novel growth method of InGaAsN dilute nitrides by MBE without the addition of Sb

^{a)}Author to whom correspondence should be addressed: baranov_art@spbau.ru

atoms is proposed to avoid the problems described above. It consists of using nanoheterostructures of an original design based on the InAs/GaAsN superlattice (SL), where several InAs monolayers (MLs) are separated by wide GaAsN barriers.²³ This technology allows to grow of InGaAsN alloys with separated fluxes of indium and nitrogen. Thus, thin InAs layers of a few monolayers compensate the elastic stresses arising during the growth of GaAsN on the GaAs wafer due to lattice-mismatch. The semiconductor compound grown by the described method is called a sub-monolayer digital alloy (SDA). The method was successfully applied for the growth of III-V^{24–26} and II-VI^{27,28} compounds by MBE.

In the current work, we present data on defects detected in SDA InGaAsN grown by MBE on GaAs wafers, in relation with the layer thickness and with single-junction SC properties. The grown photovoltaic structures are investigated by various capacitive techniques such as capacitance-voltage measurements (*C-V*), admittance spectroscopy (AS), and deep-level transient spectroscopy (DLTS). These experiments provide information on defect formation in these compounds during the growth process. The results are correlated to photoluminescence (PL) and X-ray diffraction measurements. In the future, it will help optimizing the growth conditions for dilute nitrides, which will be used as active layers in subcells of high-efficiency MJSCs.

II. EXPERIMENTS AND METHODS

Single-junction SC based on p-i-n heterostructures were grown by MBE using Veeco GenIII equipment with an RF-plasma source of nitrogen. They consist of three samples with a bottom n-type GaAs layer (200 nm thick, doping density of $3 \times 10^{18} \text{ cm}^{-3}$) first grown onto (100) n-type GaAs wafers, followed by the growth of undoped (i) InAs/GaAsN SL with different thicknesses of the active i-layer (900 nm, 1200 nm, and 1600 nm). Practically, the InAs/GaAsN SL is obtained by the growth of ternary GaAsN, 7–12 nm thick, followed by the growth of binary InAs, 0.2–0.5 nm thick (1 ML), and repeated in order to reach the targeted thickness. The top p-type layer is made of a 200 nm thick GaAs layer with a doping density of $1 \times 10^{19} \text{ cm}^{-3}$. The schematic cross-section of the samples is presented in Fig. 1. Beryllium and silicon were used for doping of the p- and n-layers in the structures, respectively. The growth process of the explored structures with layers of InAs/GaAsN grown by the SDA method is described in more detail elsewhere.²³ All samples were grown without any antireflection coating. Contacts were fabricated using photolithography and vacuum evaporation of metals. Au/Ge was used for the n-type bottom contact and Au/Zn was used for the p-type top contact. The ohmic behavior of the current-voltage characteristics for contacts was obtained after rapid thermal annealing using a Jipelec JetFirst 100 equipment. For photoelectric measurements, the top contact consisted in a grid, while for capacitance measurements, circular contacts with diameters of 0.5 and 1 mm were used on the front side; then, mesa-structures were formed by wet etching down to the wafer.

Various space charge capacitance methods were used to analyze the electronic properties of active layers grown by the

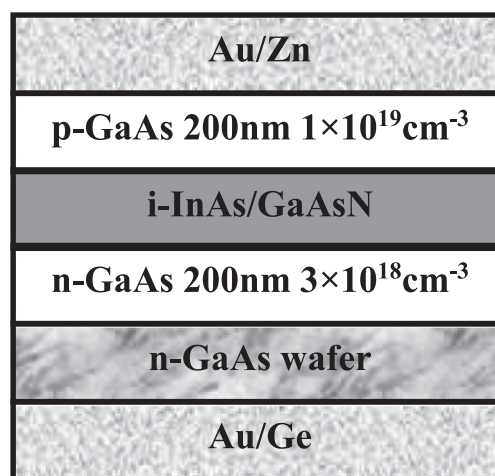


FIG. 1. Schematic view of the p-i-n structures with i-InAs/GaAsN active layers.

SDA method. First, the *C-V* characteristics were measured to define the level of doping in the layers at a frequency of 1 MHz. AS measurement was used to study the defect properties (activation energy E_a and capture cross section σ) in the layers of dilute nitrides.²⁹ Moreover, the standard DLTS³⁰ method was used to get more information about the detected defects. All capacitance measurements were performed in a liquid nitrogen vacuum cryostat in the temperature range from 77 to 400 K. The AS measurements were carried out using an RLC-meter in the frequency range from 20 Hz to 1 MHz and with a test voltage amplitude of 50 mV. *C-V* and DLTS measurements were performed using a Boonton-7200 capacitance bridge at a frequency of 1 MHz and with a test voltage amplitude of 100 mV. The AFORS-HET 2.5 software³¹ was used for numerical simulation of SC. It allows one to calculate the capacitance and photoelectrical characteristics of the SC in the one-dimensional case.³²

Samples were also characterized from photoluminescence and X-ray diffraction measurements. The energy bandgap of the active layers determined by photoluminescence was found to be 1.03 eV. Diffraction rocking curves were obtained using a DRON-8 X-ray diffractometer with a BSV 29 highly focused X-ray tube. The anode material was copper with $K\alpha 1$ radiation ($\lambda = 1.5405 \text{ \AA}$). The rocking curves were obtained in the θ - 2θ mode of scanning. The photoluminescence spectra (PL) were measured using an instrument from Accent RPM Sigma (Accent Optical Technologies) with a semiconductor laser ($\lambda = 778 \text{ nm}$) as the pumping source and at the temperature of 300 K.

Finally, the external quantum efficiency was measured at a temperature of 25 °C to study the photoelectrical properties of the structures.

III. RESULTS AND DISCUSSION

A. Quasi steady-state capacitance measurements

The *C-V* dependence was measured at reverse bias in the interval $[-1 \text{ V}, 0 \text{ V}]$ at 1 MHz and at 300 K for the three InGaAsN samples. The high frequency is chosen due to the requirement to measure only the space charge region (SCR)

capacitance and to suppress the response of potential deep defects.

The capacitance of the sample with 900 nm thick InGaAsN was found independent of the applied voltage, meaning that the effective width of the space charge region d_{eff} , probed by the capacitance measurement, defined as $d_{eff} = \epsilon/C$, with ϵ being the dielectric permittivity, is equal to the i-layer thickness. So, the i-layer is fully depleted in the 900 nm thick InGaAsN sample. As can be seen in Fig. 2(a), for the 1200 nm thick InGaAsN sample, the capacitance also tends to become constant at reverse bias, and only a very small increase is observed towards 0 V. We note that a capacitance of 10 nF/cm² corresponds to a value of d_{eff} of 1.15 μ m if we take the permittivity $\epsilon = 1.15 \times 10^{-12}$ F cm⁻¹ of GaAs, which is indeed close to the thickness of the i-InGaAsN layer. This indicates that there is no strong unintentional or residual doping in the i-layer of both 900 nm and 1200 nm thick samples. The small bias dependence on the 1200 nm thick sample does not allow us to determine the unintentional/residual doping concentration reliably from a Mott-Schottky plot. To estimate the doping concentration, we have performed electrical modeling of the sample with 1200 nm thick InGaAsN in order to simulate the *C-V* curves. From the simulated *C-V* curves with varying doping concentration (p-type, see below) [Fig. 2(a)], we can deduce that the doping concentration should be less than 1.0×10^{15} cm⁻³. For the 1.6 μ m thick InGaAsN sample, however, the capacitance is bias dependent. The experimental Mott-Schottky plot for this structure shown in Fig. 2(b) exhibits a linear behavior of $1/C^2$ as a function of the applied voltage, as expected in the depletion regime of a p-n junction. According to the slope, the effective doping concentration value is estimated at 5.0×10^{15} cm⁻³ at 300 K. Note that such a doping concentration value would have been detected even in the sample with the thinnest i-layer since the depletion capacitance would have been much larger than the geometrical capacitance because the effective space charge layer thickness would have been significantly smaller than 900 nm. In conclusion of the *C-V* measurements at room temperature, the sample with a 1600 nm thick i-layer exhibits significant higher

effective background doping than the samples with thinner i-layers. We also performed *C-V* measurements at 77 K and found that the dependence of the capacitance on applied voltage was much less pronounced, indicating that deep defects also contribute to the effective doping at 300 K. From computer simulations that will be presented below, it is found that this background doping is of acceptor type. It is worth noting that a p-type background doping is typical for i-layers of dilute nitrides (In)GaAsN grown by MBE.^{14,15} Usually, it is associated with non-equilibrium growth conditions at low temperatures that lead to the formation of gallium vacancies and nitrogen-related defects of acceptor type in dilute nitrides but a complete description and explanation of background doping in InGaAsN layers should be investigated in further experiments. Nevertheless, in our InAs/GaAsN layers, the background doping values are several times lower than those found for InGaAsN layers grown by MBE without Sb in the articles cited above (more than 1.0×10^{16} cm⁻³). Low background doping of the i-layer is necessary for better collection and transport of charge carriers in dilute nitrides with low lifetimes.^{20,33,34} Consequently, the SDA InAs/GaAsN is preferable to InGaAsN compounds grown continuously by MBE. This might be due to the ionization of defect levels giving an additional contribution to the net doping, as discussed below.

The admittance spectroscopy is based on the measurement of the capacitance and conductance of p-n or p-i-n junctions using a small signal alternating voltage at different frequencies and at various temperatures. If the Fermi level (or quasi Fermi level) crosses the defect level in the space charge region, we may detect an additional contribution to the capacitance provided that $\omega\tau < 1$, with ω being the angular frequency and τ the time response of the defect, sum of the capture and emission frequencies which are equal at the quasi Fermi level. This leads to a step-like behavior in the capacitance versus temperature, $C(T)$, or capacitance versus frequency, $C(f)$, curve. Therefore, admittance spectroscopy can detect responses coming from the i-InAs/GaAsN layer, even if the layer is fully depleted, the high frequency/low temperature capacitance value being then determined by the

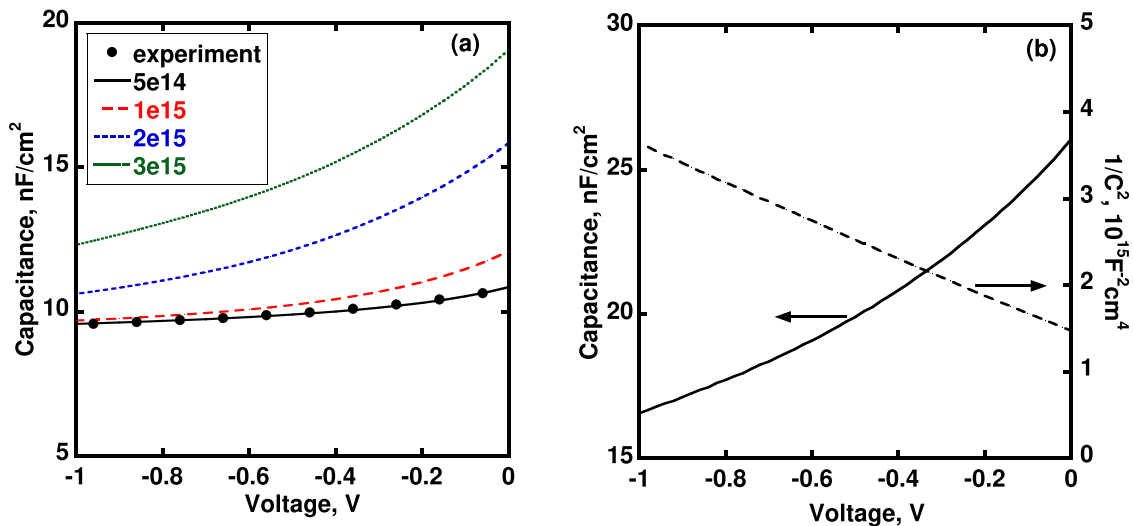


FIG. 2. Capacitance-voltage (*C-V*) characteristics measured for the 1.2 μ m thick InGaAsN sample and simulated with varying doping concentration (in cm⁻³) (a) and *C-V* and Mott-Schottky plot for the 1.6 μ m thick InGaAsN sample (b). Experimental and simulated data were obtained at 300 K and at 1 MHz.

i-layer thickness. The step position, or turn-on, is defined as $\omega_t\tau = 1$, which leads to

$$\frac{f_t}{T_t^2} = \frac{v_{300}N_{300}\sigma}{\pi(300)^2} \exp\left(-\frac{E_a}{k_B T_t}\right), \quad (1)$$

where f_t is the turn-on frequency, T_t is the turn-on temperature, k_B is the Boltzmann constant, E_a is the escape energy of a majority carrier from the defect to its band, v_{300} and N_{300} are the thermal velocity and effective density in the band at 300 K, respectively, and σ is the capture cross section of the defect for the majority carrier.²⁹ From Eq. (1), it is obvious that the step position in a C vs f plot is shifted to higher frequency when the temperature is increased. The step in the capacitance is also accompanied by a maximum in the conductance, which is a simple way to clearly identify the turn-on angular frequency, ω_t . However, the maximum in the conductance is often hidden by the parasitic shunt conductance or the dc conductance related to the current flow across the junction that increases with temperature. This is why conductance values will not be presented here. The turn-on position can then be determined at a given temperature in a capacitance vs frequency plot, by the

maximum of the capacitance derivative dC/df or preferentially the maximum of the so-called differential capacitance $dC/d[\ln(f)]$. Indeed, it can be seen from Eq. (1) that a change in temperature is equivalent to a change in the logarithm of frequency (apart from the T^2 dependence that only introduces a second order deviation) in the definition of the energy scale of the detected defect level. The temperature and frequency dependences of the raw and differential capacitance of our InGaAsN structures are shown in Fig. 3 for zero bias voltage. The capacitance of the sample with the 1200 nm thick InGaAsN layer exhibits two steps [Fig. 3(a)] that are evidenced in the peaks of the differential capacitance $f \times dC/df$ [Fig. 3(c)]. We can observe a first step on $C(f)$ leading to a peak on $f \times dC/df$ at low temperatures 100–280 K and a second one at higher temperatures, 320–360 K (the series of steps are indicated by arrows). These steps can be caused either by interface states at the InGaAsN/GaAs heterojunction or by bulk defect levels in the i-layer. The $C(T, f)$ curves were measured at different applied bias voltages (measurements are not shown here) and the step position in $C(f)$ curves does not change: it indicates that the response originates from bulk defects rather than from the interface. Further increase in thickness of the

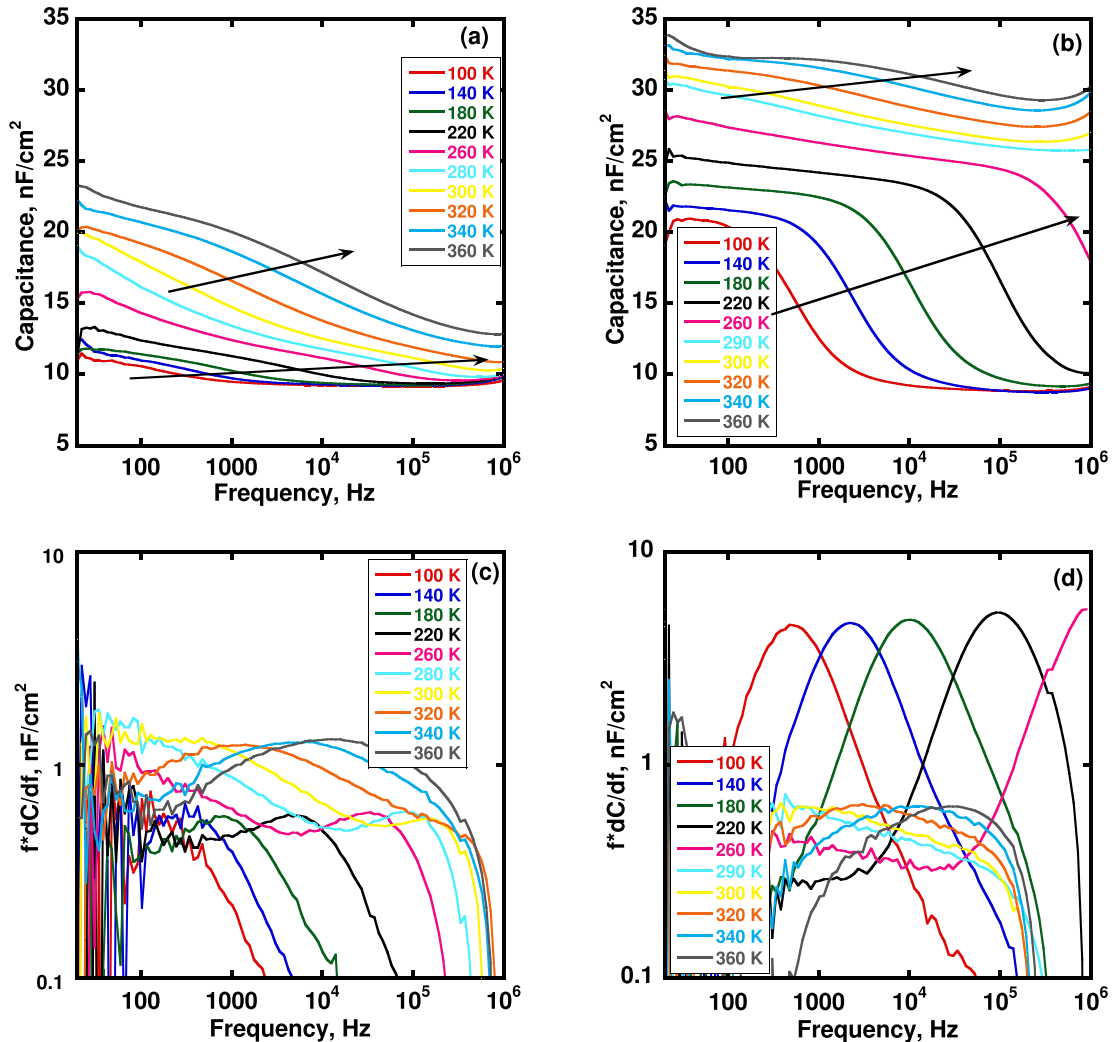


FIG. 3. Frequency dependent capacitance, C , (top) and differential capacitance, $f \times dC/df$, (bottom) at various temperatures for zero bias voltage, measured on SC with InGaAsN active layers with thicknesses of 1200 nm (a), (c), and 1600 nm (b), (d).

InGaAsN layer up to 1600 nm leads to a drastic enlargement of the amplitude of the first step while the second step in $C(f)$ curves remains the same [Fig. 3(b)].

Defect parameters (E_a and σ) in InAs/GaAsN were extracted from Arrhenius plots of f_i/T_i^2 , according to Eq. (1). Note that, while the error in the energy determination can be evaluated at ± 0.05 eV, the error in the determination of σ is quite large due to the extraction procedure (a small change in the slope of the linear fit induces a strong change in σ). In addition, the values of thermal velocity and effective density of states (DOS) in the band are not well known in these new III-V compounds, but they are calculated from effective mass of $m_e = 0.1 \times m_0$ and $m_h = 0.47 \times m_0$ for InGaAsN compounds. The characteristic Arrhenius plots for extraction of defect parameters in our samples are shown in Fig. 4.

For the sample with an i-layer thickness of 1200 nm, the defect level revealed at low temperature has characteristic values $E_a = 0.20$ eV and $\sigma = 3 \times 10^{-17}$ cm², while the defect revealed at high temperature has parameters $E_a = 0.46$ eV and $\sigma = 1.4 \times 10^{-15}$ cm². For the sample with a 1600 nm thick i-layer, we find $E_a = 0.18$ eV and $\sigma = 1.4 \times 10^{-16}$ cm² for the low-temperature defect level, while for the high-temperature one, we find $E_a = 0.54$ eV and $\sigma = 3.4 \times 10^{-14}$ cm². The defect parameters are presented in Table I. Taking into account the above-mentioned uncertainties in the extracted defect parameter values, we can conclude that the defects detected in both 1200 nm and 1600 nm thick samples are likely to be the same and constitute a characteristic feature of the i-InGaAsN layer based on the InAs/GaAsN SDA.

According to measured $C(T, f)$ data, we can conclude that layers of InGaAsN grown using InAs/GaAsN SDA do not exhibit any response from defects so their concentration is below the detection limit of the AS technique up to at least a thickness of 900 nm (not shown here). Further, when the

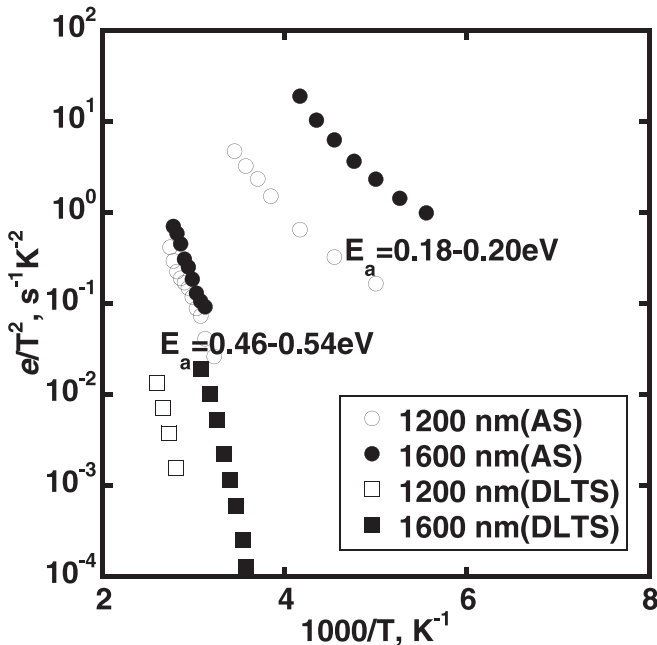


FIG. 4. Characteristic Arrhenius plots for extraction of defect parameters by AS (circles) and DLTS (squares) for the InAs/GaAsN samples with thicknesses of 1200 nm (open symbols) and 1600 nm (full symbols).

TABLE I. Parameters of defects detected in i-InAs/GaAsN samples.

Thickness, nm	E_a , eV	σ , cm ²	N_T , cm ⁻³	Method
1200	0.20	3.0×10^{-17}	5.0×10^{14}	AS
	0.46	1.4×10^{-15}	8.4×10^{14}	AS
	0.82	4.5×10^{-13}	n/e	DLTS
	0.18	1.4×10^{-16}	3.5×10^{15}	AS
1600	0.54	3.4×10^{-14}	1.3×10^{15}	AS
	0.78	1.9×10^{-11}	1.0×10^{15}	DLTS

thickness is increased to 1200 nm, conditions become more favorable for the formation of defects in InGaAsN but their concentration is still low, so it does not lead to a drastic change in the capacitance curves [Fig. 3(a)]. However, the defect concentration drastically increases when the thickness is increased to 1600 nm, leading to huge changes in the capacitance-frequency curves [Fig. 3(b)]. Such behavior of defects in epitaxial multilayers which have a small lattice misfit with the wafer was widely discussed.^{35,36} It was shown that a misfit will be accommodated by a uniform elastic strain until a critical film thickness is reached. Thereafter, it is energetically favorable for the misfit to be shared between dislocations and the strain. Thus, we can propose that a 900 nm thick layer is strained and has a low defect concentration, while increase in the layer thickness to 1200 nm leads to dislocation formation and therefore defect responses are detected.

In the following, we estimate the concentration of detected defects in samples with i-InGaAsN thicknesses of 1200 nm and 1600 nm. To this purpose, the method suggested by Walter was used.³⁷ It is based on the use of the capacitance derivative with respect to angular frequency. The density of states (DOS) can be reconstructed by this method for both p-n and p-i-n junctions. In Fig. 5 we present the DOS corresponding to the detected defects. The total defect concentration (N_T) was estimated for the p-i-n junction case from the integration of the DOS over the defect distribution around 0.18–0.20 eV. We found $N_T = 5 \times 10^{14}$ cm⁻³ and $N_T = 3.5 \times 10^{15}$ cm⁻³ for samples with i-InGaAsN 1200 nm and 1600 nm thick, respectively (Table I). These values are close to that of the effective doping concentrations estimated from C-V measurements at 300 K. Consequently, the observed shallow defects completely ionize at temperatures above 260 K introducing an additional charge that can explain the observed increase in the effective doping concentration at 300 K in the sample with the largest thickness. A peak in the DOS is also obtained around 0.50 eV, as shown in Fig. 5. The estimated defect concentration is slightly lower for the sample with InGaAsN 1200 nm thick (8.4×10^{14} cm⁻³) than with 1600 nm (1.3×10^{15} cm⁻³) (Table I).

B. DLTS measurements

The samples were also explored by the DLTS technique with the following conditions: the amplitude of the reverse bias voltage was $V_{rev} = -1$ V, the amplitude of the filling pulse was $V_{pulse} = 1$ V (i.e., the voltage during the filling pulse was 0 V), and the filling pulse duration was $t_{pulse} = 40$ ms. The DLTS spectra $S(T)$ for different rate windows is shown in

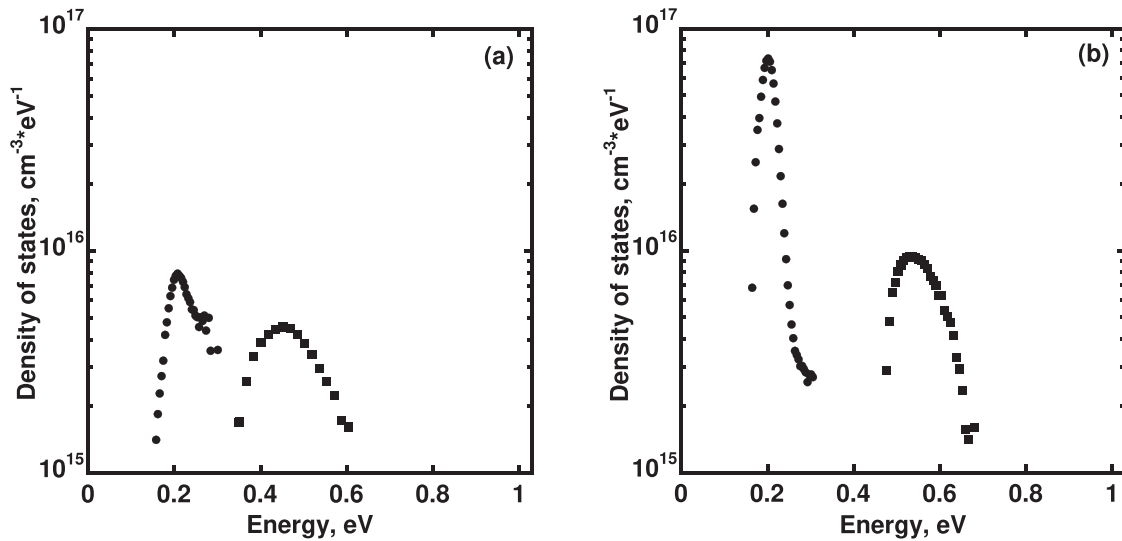


FIG. 5. Density of states in the energy bandgap for low (circles) and high (squares) temperature defects detected by admittance spectroscopy for 1200 nm (a) and 1600 nm (b) thick i-InGaAsN layers.

Fig. 6. No peaks are detected in the DLTS spectrum for the used temperature range in the 900 nm thick InGaAsN sample [Fig. 6(a)]. On the other hand, peaks of the capacitance are observed for the 1200 nm thick sample at temperatures above 360 K and high emission rates [Fig. 6(b)]. The position of the peaks shifts toward higher temperatures when the rate window is increased, but their amplitude also substantially increases and their shape is quite broad. A series of broad peaks with a much larger amplitude is observed in the 1600 nm thick sample at temperatures 280–360 K. Such broad peaks are usually assigned to extended defects such as dislocations rather than to point defects.³⁸

The Arrhenius plots of defects obtained from the DLTS spectra are shown in Fig. 4 in order to compare with the AS data. The defect parameters extracted from both techniques are presented in Table I. The important difference in AS and DLTS measurements is the different used range of emission rates, because the DLTS setup with Boonton-7200 allows to accurately measure capacitance transients with relatively low emission rates, $e < 2000 \text{ s}^{-1}$, unlike AS that can better reveal higher emission rates. From DLTS measurement, we found an activation energy around $E_a \sim 0.8 \text{ eV}$ and a cross section around $\sigma \sim 10^{-15} \text{ cm}^2$ for the defect state. We could relate this defect state to that deep-defect one measured using AS. However, the difference between the values of E_a measured by the two techniques ($\sim 0.8 \text{ eV}$ vs $\sim 0.5 \text{ eV}$ using DLTS and AS, respectively) is large and remains unclear. Using DLTS, such high activation energy had already been detected in similar materials,^{39,40} but no explanation about the large E_a value (larger than half of the bandgap) was given. Further research should be done to resolve why the activation energy evaluated from DLTS is much higher than the midgap. It is an unexpected and unusual result which forces to consider DLTS data carefully and with a critical view. Admittance spectroscopy is likely to be more suitable to extract defect parameters in our layers where doping is low, unintentional, and related to shallow defects. Indeed, in DLTS, the dopant concentration should be higher than the deep defect concentration for correct

interpretation of the data. This may explain the discrepancy between the defect parameters extracted from AS and DLTS, along with the unexpected large activation energies from DLTS.

The absence of responses from the low-temperature level on the DLTS spectra can be explained by the principle of DLTS measurement in the case of fully depleted i-InAs/GaAsN in p-i-n junctions at low temperature for all samples. In this case, when the applied voltage returns at reverse value following the filling pulse, the space charge region must extend in adjacent layers in the structure. But the cover layers of p- and n-GaAs have very high doping concentration ($1 \times 10^{19} \text{ cm}^{-3}$ and $3 \times 10^{18} \text{ cm}^{-3}$) so the DLTS signal should be low because although it is proportional to the defect density, it is also inversely proportional to the doping density at the edge of the space charge layer.³⁰ This may also explain the absence of high temperature response in the sample with the 1200 nm thick i-InGaAsN layer in DLTS spectra. However, the sample with 1600 nm thick InGaAsN rather behaves as a p-n junction at temperatures above 240 K due to additional ionization of shallow defects. Nevertheless, the low activation energy of this defect ($E_a = 0.20 \text{ eV}$) does not allow considering it as an effective center of non-radiative recombination that could be responsible for low lifetimes in the layers of dilute nitrides InAs/GaAsN (see below).

On the contrary, defects detected at high temperature ($E_a = 0.45\text{--}0.55 \text{ eV}$) are close to the middle of the bandgap of the InGaAsN ($E_g = 1.03 \text{ eV}$) and have large capture cross sections so they can have a strong influence on the charge carriers lifetimes in active layers of SC. Defects with similar parameters were previously observed in many studies.^{15,39,41,42} Broad DLTS peaks in Fig. 6(c) mean non-exponential response compared to the classical case of DLTS spectra for a point defect, so the interpretation of data should be considered more carefully. Broad shape and increasing amplitude of peaks can be due to different causes: local fluctuations in the composition of the compounds,⁴³ overlap of responses from several discrete defect levels with small separation in energy, defects having an energy density of states (e.g. Gaussian distribution, extended

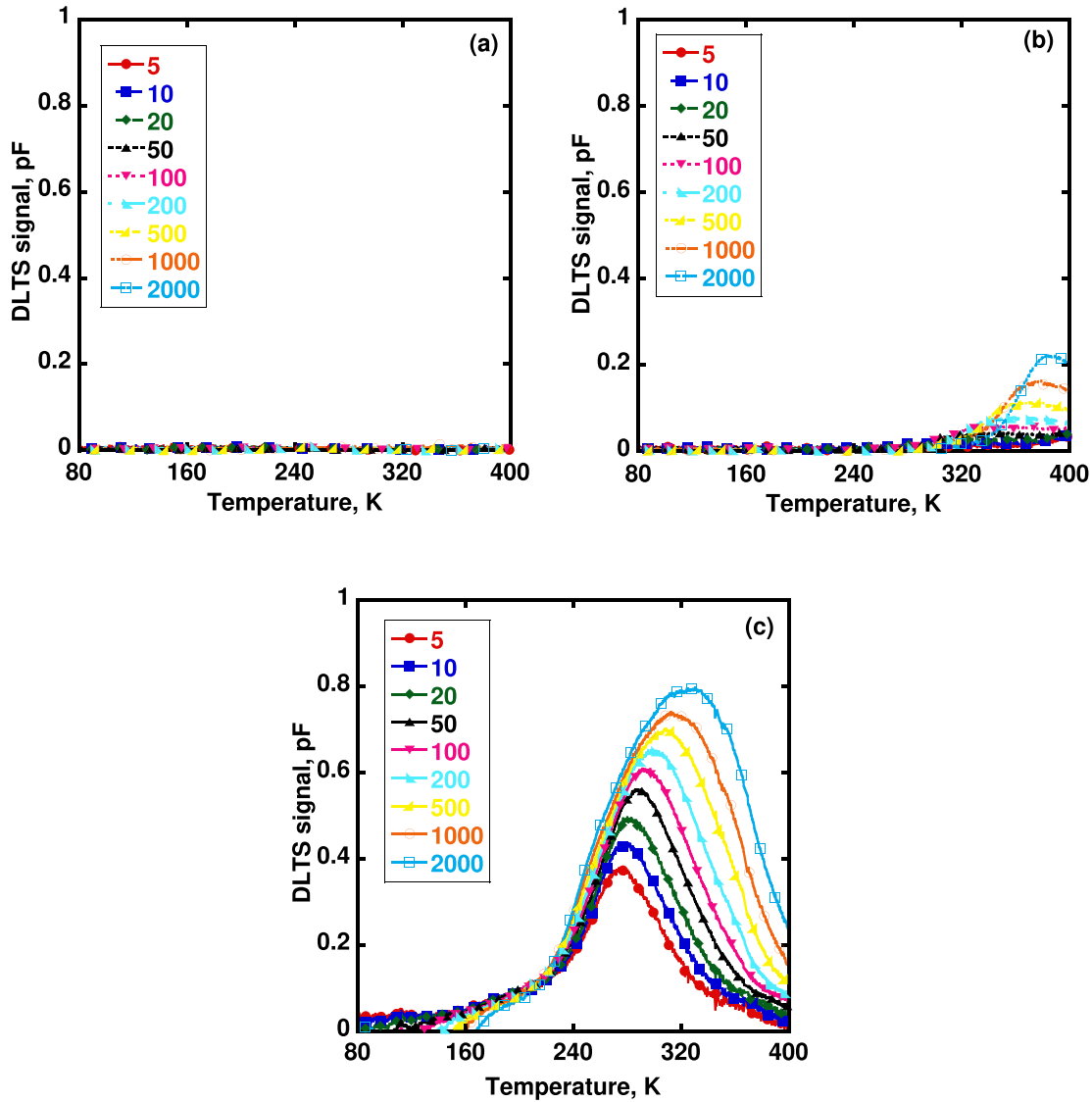


FIG. 6. DLTS spectra $S(T)$ on solar cell structures made of active layers of InAs/GaAsN with thicknesses of 900 nm (a), 1200 nm (b), and 1600 nm (c) for different rate windows (in s^{-1}).

defects with unknown energy distribution), dislocations, etc. In Ref. 36, a convenient method was proposed for analyzing such responses from extended defects (not point defects with discrete energy level) that exist with localized and band-like states. For the InGaAsN alloys grown by MBE with a RF-plasma source of nitrogen, the analysis shows logarithmic enlargement of the peak amplitude without any temperature shift when the duration of the filling pulse is increased until up to 10 ms for the same rate window: such behavior is typical for localized states.¹⁵ However, saturation occurs at t_{pulse} larger than 10 ms and the peak amplitude remains constant like in case of a point defect. Probably, in the case of dilute nitrides, a strong fluctuation in composition occurs due to nonequilibrium growth conditions and the tendency of nitrogen clusterization leads to the transformation of point defects into extended ones with some energy distribution.

C. Photoluminescence and X-ray diffraction

The photoluminescence (PL) spectra of the InGaAsN samples measured at room temperature are displayed in Fig. 7.

The bandgap energy is 1.03 eV whatever the sample thickness. However, we observe that the intensity of photoluminescence strongly decreases when the thickness increases. This is consistent with the increasing defect density derived from previous capacitance measurements. Indeed, deep defects act as non-radiative recombination centers that reduce the free carrier concentrations, thus also reducing the band-to-band PL signal.

Further correlation to previous measurements supporting the increase in defects with increasing thickness is provided by X-ray diffraction measurements (Fig. 8). The main peak is related to the response from the GaAs wafer, and the peak at a slightly smaller angle is attributed to the InGaAsN layer. This indicates that InGaAsN is under compressive stress and presents a slightly larger average lattice constant than GaAs. We observe that the shift of the peak is increased with the thickness, especially for the 1600 nm thick layer, where it becomes strongly broadened, indicating partial relaxation and formation of defects and dislocations. Formation of dislocations and other defects are known to occur in thick

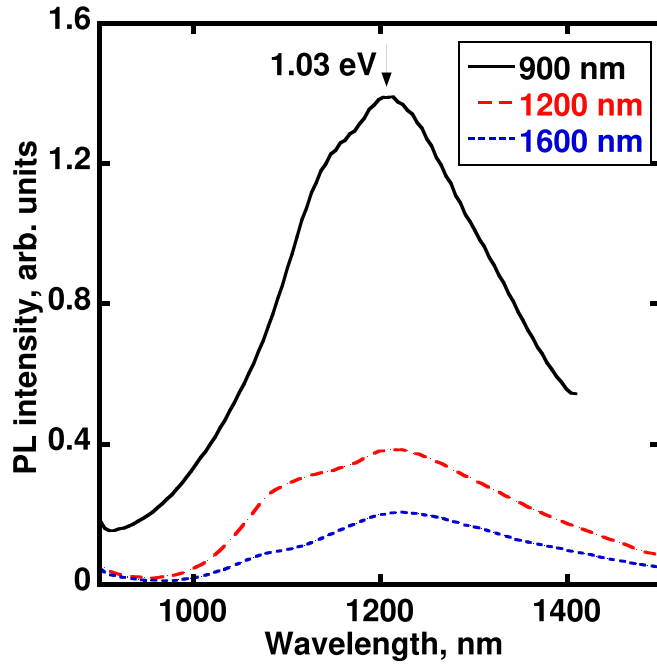


FIG. 7. Photoluminescence spectra of the 900 nm, 1200 nm, and 1600 nm thick InGaAsN samples.

strained layers when it exceeds the critical thickness in heteroepitaxial growth.^{44,45}

D. External quantum efficiency of solar cells

The external quantum efficiency (EQE) of the solar cell with an active layer of InGaAsN drastically drops when the layer thickness increases from 1200 nm to 1600 nm [Fig. 9(a)].

The drop in EQE occurs when photogenerated electron-hole pairs cannot effectively reach the highly doped GaAs

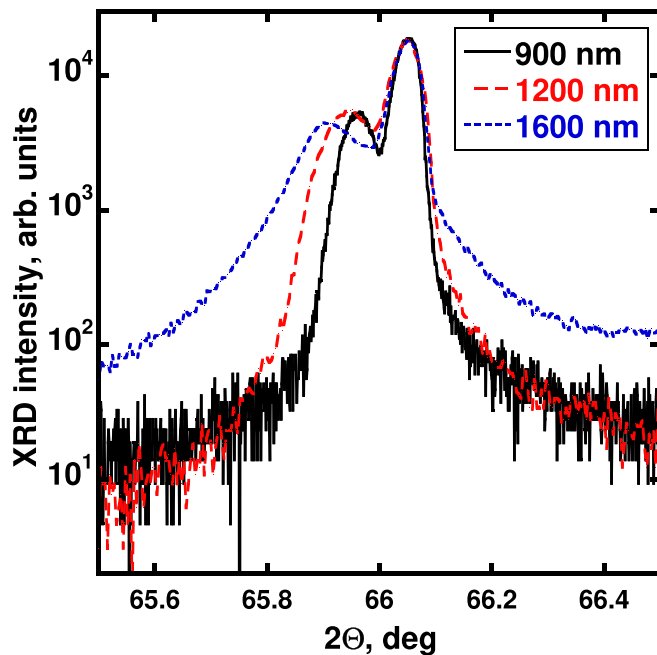


FIG. 8. X-ray-diffraction rocking curves of the 900 nm, 1200 nm, and 1600 nm thick InGaAsN samples.

layers and recombine in the InGaAsN active one. In principle, in a p+-i-n+ structure, the built-in electric field in the active i-layer improves the separation and collection of charge carriers and reduces recombination in the active region of the solar cell. However, the presence of a background doping and of charged defects which were revealed in our layers from the capacitance measurements tends to replace the p+-i-n+ structure by either a p+-n-n+ or a p+-p-n+ structure. In the first case, the p-n junction is the top p+-GaAs/n-InGaAsN junction, while in the second case, it is the bottom p-InGaAsN/n+-GaAs junction. In order to investigate these two possibilities, we performed numerical simulations using AFORS-HET 2.5. To simulate either the n-InGaAsN case or the p-InGaAsN case, we introduce either a donor type defect at 0.18 eV below the conduction band or an acceptor type defect at 0.18 eV above the valence band (as detected from admittance spectroscopy) with a concentration of $5 \times 10^{15} \text{ cm}^{-3}$ (that was obtained from the C-V analysis at 300 K for the 1600 nm thick InGaAsN sample). Simulated band diagrams for n- and p-InGaAsN are presented in Figs. 10(a) and 10(b), respectively. Also, the EQE curves were calculated taking into account the reflection losses that were measured on solar cells [Fig. 9(b)]. We introduced a bulk defect level located at 0.5 eV below the conduction band in n-InGaAsN (above the valence band edge in p-InGaAsN), with capture cross sections of electrons and holes equal to $2 \times 10^{-13} \text{ cm}^2$ and $2 \times 10^{-14} \text{ cm}^2$, respectively. The defect concentration was varied for both cases [Figs. 10(c) and 10(d), respectively]. In the first case, the separation of charge carriers generated at short wavelength will occur more efficiently, since the regions of high built-in electric field and high absorption (close to the front surface) coincide. In the second case, these regions are spatially separated. As a consequence, the EQE is more affected in the second case due to enhanced recombination of electron-hole pairs and the shape of the EQE curve is different. The big drop in EQE observed in the 1600 nm-InGaAsN sample is more pronounced at short wavelength, where light is absorbed in a narrow depth close to the p+-GaAs/i-InGaAsN interface. This behavior is well reproduced in the simulation if the InGaAsN layer is of p-type. This suggests that the InGaAsN layer has a p-type background doping and that the p-n junction is located at the bottom side. Therefore, all detected defects from AS and DLTS are traps for holes because they are majority carrier traps in p-InGaAsN. Another consequence is that the defects in the 1600 nm thick sample were detected at the bottom side of InGaAsN, indicating that increasing the thickness from 900 nm to 1600 nm has produced defects not only in the upper part of the layer, but the defects are likely to be distributed all over the thickness.

Taking now the InGaAsN layer to be p-type, we also simulated the EQE curve for various deep defect concentrations for 900 nm and 1200 nm thick samples (Fig. 11). An increase in the thickness of the InGaAsN layer from 900 nm to 1200 nm leads to only very small changes in the EQE curve: a small increase in the long-wavelength range because of enhanced absorption. The increase in the defect concentration up to $0.5 \times 10^{15} \text{ cm}^{-3}$ induces a small decrease in EQE because the electric field is strong enough in the InGaAsN layer to separate the carriers and to allow

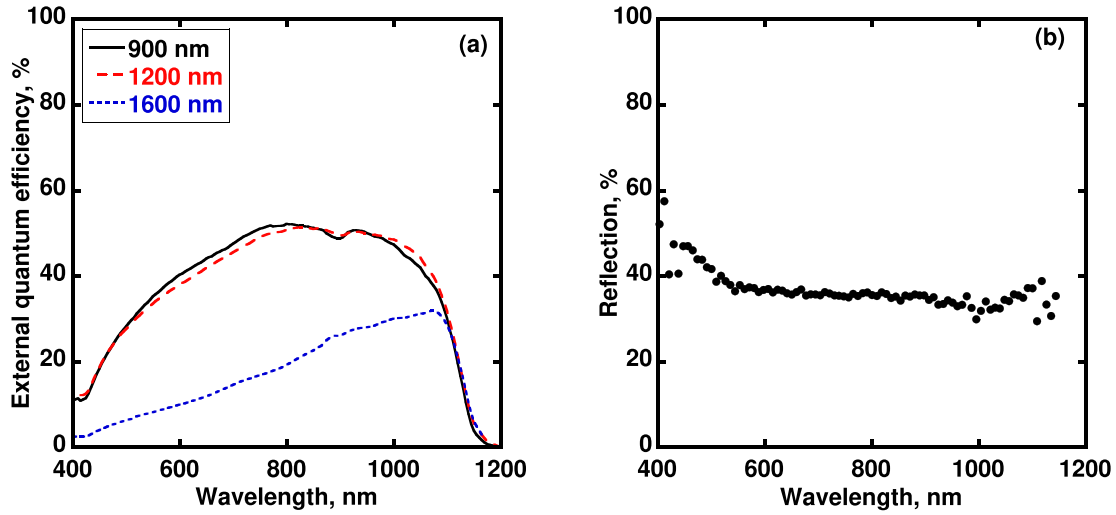


FIG. 9. Measured external quantum efficiency (a) and reflection (b) of single-junction SCs with i-InGaAsN.

them to be collected before they recombine. On the contrary, for the 1600 nm thick InGaAsN layer, the EQE curve exhibits the drastic decrease at short wavelength and the same shape as observed experimentally when the defect

concentration is above $0.5 \times 10^{15} \text{ cm}^{-3}$. Therefore, the concentration of $(0.5-2) \times 10^{15} \text{ cm}^{-3}$ estimated from AS and DLTS allows to achieve good qualitative and quantitative correlation between experiments and simulations.

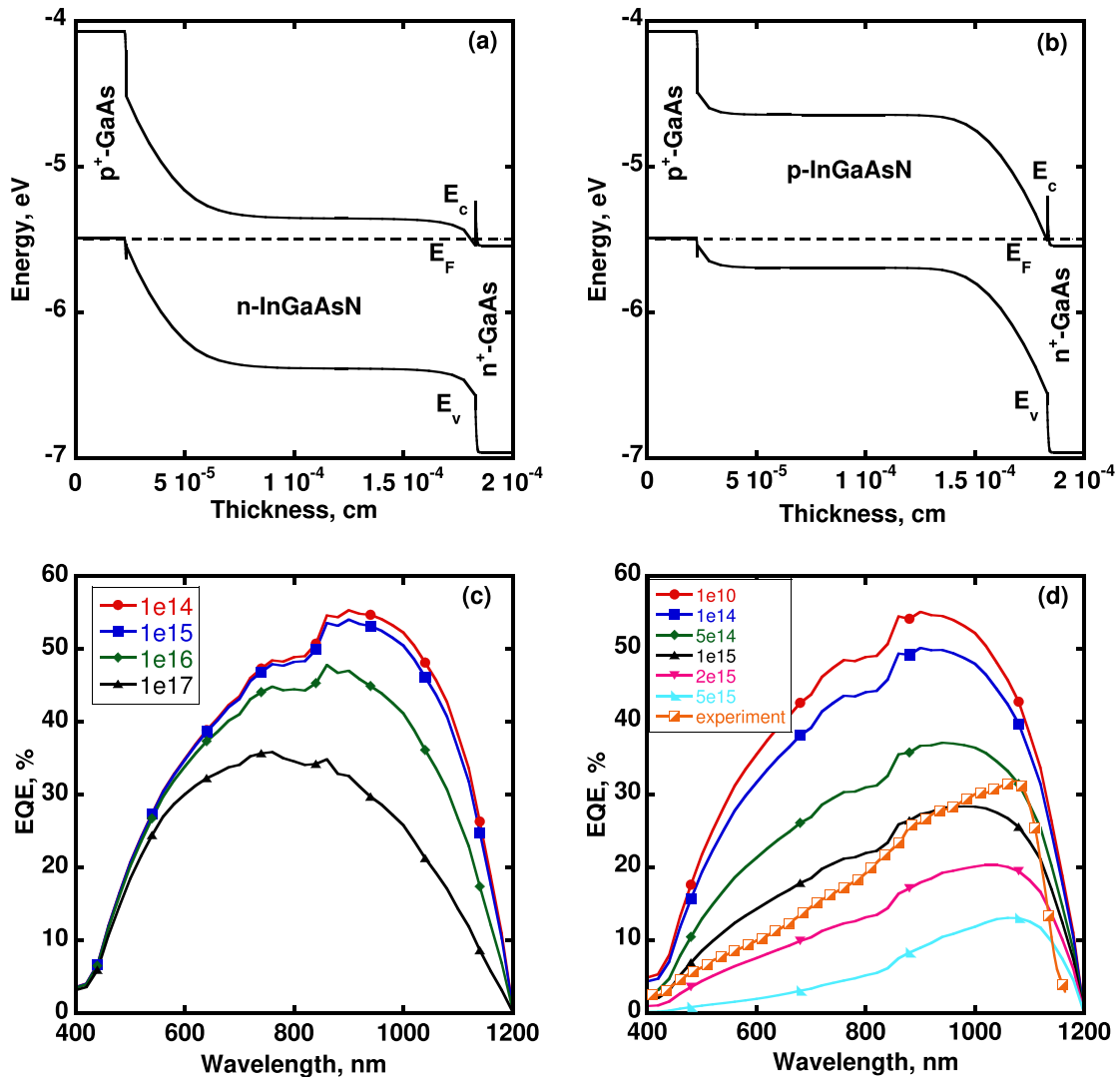


FIG. 10. Band diagram of modeled p+-GaAs/n-InGaAsN/n+-GaAs (a) and p+-GaAs/p-InGaAsN/n+-GaAs (b) structures with the 1600 nm thick InGaAsN layer, and corresponding external quantum efficiency for various deep defect concentrations (in cm^{-3}) (c) and (d). The experimental curve is also shown in (d).

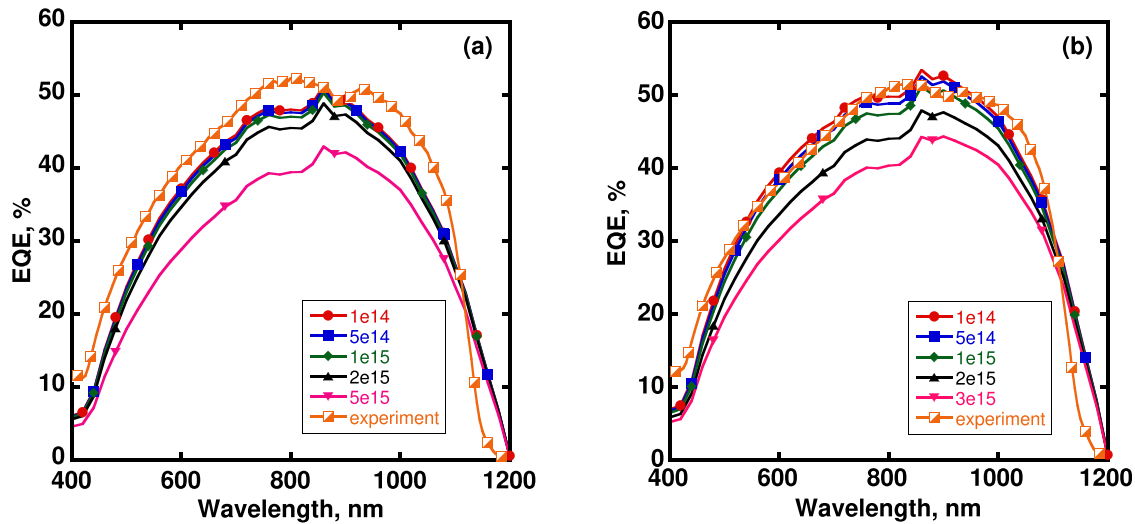


FIG. 11. Measured and simulated external quantum efficiency curves of the p-i-n structures with InGaAsN 900 nm (a) and 1200 nm (b) thick for various deep defect concentrations (in cm^{-3}).

Consequently, the relation was demonstrated between the thickness of the i-InGaAsN active layer grown by MBE in the form of SDA InAs/GaAsN in solar cells and their photoelectric and internal properties. An increase in the thickness of the active layer leads to formation of defects that are centers of non-radiative recombination, responsible for a strong drop in EQE in the short-wavelength region.

IV. CONCLUSION

Different capacitance methods (C-V, AS, and DLTS), as well as photoluminescence and XRD measurements, were used to study i-layers of InGaAsN dilute nitrides grown as sub-monolayer digital alloys based on the InAs/GaAsN superlattice by molecular beam epitaxy on GaAs wafers for applications in multi-junction solar cells. Low p-type background doping was demonstrated at room temperature in the 900 nm and 1200 nm thick layers. Increasing the thickness from 900 nm to 1200 nm leads to the formation of centers of non-radiative recombination with an activation energy of 0.5 eV ($N_T = 8.4 \times 10^{14} \text{ cm}^{-3}$) and a shallow defect level at 0.20 eV. The latter also contributes to doping but its concentration is low ($N_T = 5 \times 10^{14} \text{ cm}^{-3}$) so it does not strongly affect the band diagram and the external quantum efficiency of solar cells. A further increase in thickness to 1600 nm leads to significant increase in the shallow defect concentration, up to $(3-5) \times 10^{15} \text{ cm}^{-3}$, while the concentration of deep levels becomes higher ($1.3 \times 10^{15} \text{ cm}^{-3}$). Therefore, additional free charge carriers from the shallow level doping effect change the band diagram from p-i-n to p-n junction at room temperature and the external quantum efficiency is drastically reduced due to the loss of electric field in most part of the i-layer and to the influence of non-radiative recombination centers.

ACKNOWLEDGMENTS

The reported study was carried out in the framework of the research project for young scientists RFBR #16-38-00791 and the PACSiFIC project funded by the RFBR (#16-58-150006) and the CNRS (PRC No. 1062). Artem Baranov

wants to thank the French government and Campus France (bourse Metchnikov) and Université Paris-Sud for the financial and administrative support during his Ph.D. thesis under joint Russian-French supervision.

- ¹M. A. Green, Y. Hishikawa, W. Warta, E. D. Dunlop, D. H. Levi, J. Hohl-Ebinger, and A. W. H. Ho-Baillie, *Prog. Photovoltaics* **25**, 668 (2017).
- ²F. Dimroth, M. Grave, P. Beutel, U. Fiedeler, C. Karcher, T. N. D. Tibbits, E. Oliva, G. Siefer, M. Schachtner, A. Wekkeli, A. W. Bett, R. Krause, M. Piccin, N. Blanc, C. Drazek, E. Guiot, B. Ghyselen, T. Salvétat, A. Tauzin, T. Signamarcheix, A. Dobrich, T. Hannappel, and K. Schwarzburg, *Prog. Photovoltaics* **22**, 277 (2014).
- ³K. Sasaki, T. Agui, K. Nakaido, N. Takahashi, R. Onitsuka, and T. Takamoto, *AIP Conf. Proc.* **1556**, 22–25 (2013).
- ⁴NREL Press Release NR-4514, 16 December 2014.
- ⁵R. R. King, D. C. Law, K. M. Edmondson, C. M. Fetzer, G. S. Kinsey, H. Yoon, R. A. Sherif, and N. H. Karam, *Appl. Phys. Lett.* **90**, 183516 (2007).
- ⁶S. R. Kurtz, D. Myers, and J. M. Olson, in *Conference Record of the 26th IEEE Photovoltaics Specialists Conference, Anaheim, California* (1997), pp. 875–878.
- ⁷M. Yamaguchi, K. I. Nishimura, T. Sasaki, H. Suzuki, K. Arafune, N. Kojima, Y. Ohsita, Y. Okada, A. Yamamoto, T. Takamoto, and K. Araki, *Sol. Energy* **82**, 173 (2008).
- ⁸M. Weyers, M. Sato, and H. Ando, *Jpn. J. Appl. Phys., Part 2* **31**, L853 (1992).
- ⁹J. Allen, V. Sabnis, M. Wiemer, and H. Yuen, in 9th International Conference on Concentrator Photovoltaic Systems, Miyazaki, Japan (2013).
- ¹⁰A. Aho, R. Isoaho, A. Tukiainen, V. Polojärvi, T. Aho, M. Raappana, and M. Guina, *AIP Conf. Proc.* **1679**, 050001 (2015).
- ¹¹R. Campesato, A. Tukiainen, A. Aho, G. Gori, R. Isoaho, E. Greco, and M. Guina, in *E3S Web Conference*, edited by A. Fernandez (*EDP Sciences*, 2017), Vol. 16 p. 3003.
- ¹²A. Tukiainen, A. Aho, G. Gori, V. Polojärvi, M. Casale, E. Greco, R. Isoaho, T. Aho, M. Raappana, R. Campesato, and M. Guina, *Prog. Photovoltaics* **24**, 914 (2016).
- ¹³S. Kurtz, S. W. Johnston, J. F. Geisz, D. J. Friedman, and A. J. Ptak, in 31st IEEE Photovoltaics Specialists Conference and Exhibition, Lake Buena Vista, Florida (2005).
- ¹⁴B. Bouzazi, H. Suzuki, N. Kojima, Y. Ohsita, and M. Yamaguchi, *Jpn. J. Appl. Phys.* **49**, 121001 (2010).
- ¹⁵V. Polojärvi, A. Aho, A. Tukiainen, M. Raappana, T. Aho, A. Schramm, and M. Guina, *Sol. Energy Mater. Sol. Cells* **149**, 213 (2016).
- ¹⁶S. Kurtz, A. A. Allerman, E. D. Jones, J. M. Gee, J. J. Banas, and B. E. Hammons, *Appl. Phys. Lett.* **74**, 729 (1999).
- ¹⁷N. Miyashita, N. Ahsan, and Y. Okada, *Phys. Status Solidi A* **214**, 1600586 (2017).

- ¹⁸K. Volz, D. Lackner, I. Németh, B. Kunert, W. Stolz, C. Baur, F. Dimroth, and A. W. Bett, *J. Cryst. Growth* **310**, 2222 (2008).
- ¹⁹M. M. Islam, N. Miyashita, N. Ahsan, T. Sakurai, K. Akimoto, and Y. Okada, *Appl. Phys. Lett.* **105**, 112103 (2014).
- ²⁰N. Miyashita, N. Ahsan, and Y. Okada, *Prog. Photovoltaics* **24**, 28 (2016).
- ²¹D. B. Jackrel, S. R. Bank, H. B. Yuen, M. A. Wistey, J. S. Harris, A. J. Ptak, S. W. Johnston, D. J. Friedman, and S. R. Kurtz, *J. Appl. Phys.* **101**, 114916 (2007).
- ²²V. Polojärvi, A. Aho, A. Tukiainen, A. Schramm, and M. Guina, *Appl. Phys. Lett.* **108**, 122104 (2016).
- ²³E. V. Nikitina, A. S. Gudovskikh, A. A. Lazarenko, E. V. Pirogov, M. S. Sobolev, K. S. Zelentsov, I. A. Morozov, and A. Y. Egorov, *Semiconductors* **50**, 652 (2016).
- ²⁴M. Sato and Y. Horikoshi, *J. Appl. Phys.* **66**, 851 (1989).
- ²⁵R. Cingolani, O. Brandt, L. Tapfer, G. Scamarcio, G. C. La Rocca, and K. Ploog, *Phys. Rev. B* **42**, 3209 (1990).
- ²⁶A. Y. Egorov, A. E. Zhukov, P. S. Kop'ev, N. N. Ledentsov, M. V. Maksimov, and V. M. Ustinov, *Semiconductors* **28**, 363 (1994).
- ²⁷S. V. Ivanov, A. A. Toropov, T. V. Shubina, A. V. Lebedev, S. V. Sorokin, A. A. Sitnikova, P. S. Kop'ev, G. Reuscher, M. Keim, F. Bensing, A. Waag, G. Landwehr, G. Pozina, J. P. Bergman, and B. Monemar, *J. Cryst. Growth* **214–215**, 109 (2000).
- ²⁸S. V. Ivanov, O. V. Nekrutkina, S. V. Sorokin, V. A. Kaygorodov, T. V. Shubina, A. A. Toropov, P. S. Kop'ev, G. Reuscher, V. Wagner, J. Geurts, A. Waag, and G. Landwehr, *Appl. Phys. Lett.* **78**, 404 (2001).
- ²⁹D. L. Losee, *J. Appl. Phys.* **46**, 2204 (1975).
- ³⁰D. V. Lang, *J. Appl. Phys.* **45**, 3023 (1974).
- ³¹W. G. J. H. M. Van Sark, L. Korte, and F. Roca, *Physics and Technology of Amorphous-Crystalline Heterostructure Silicon Solar Cells* (Springer, Berlin, Heidelberg, 2012).
- ³²R. Varache, C. Leendertz, M. E. Gueunier-Farret, J. Haschke, D. Muñoz, and L. Korte, *Sol. Energy Mater. Sol. Cells* **141**, 14 (2015).
- ³³J. F. Geisz, J. M. Olson, D. J. Friedman, K. M. Jones, R. C. Reedy, and M. J. Romero, in *Proceedings of the 31st IEEE PVSC* (2005), pp. 695–698.
- ³⁴A. I. Baranov, A. S. Gudovskikh, E. V. Nikitina, and A. Y. Egorov, *Tech. Phys. Lett.* **39**, 1117 (2013).
- ³⁵F. C. Frank and J. H. van der Merwe, *Proc. R. Soc. A: Math. Phys. Eng. Sci.* **198**, 216 (1949).
- ³⁶J. H. Van Der Merwe, *J. Appl. Phys.* **34**, 117 (1963).
- ³⁷T. Walter, R. Herberholz, C. Müller, and H. W. Schock, *J. Appl. Phys.* **80**, 4411 (1996).
- ³⁸M. Dąbrowska-Szata, G. Jóźwiak, and Ł. Gelczuk, *Mater. Sci.* **23**, 625 (2005).
- ³⁹S. W. Johnston, R. Ahenkiel, A. Ptak, D. Friedman, and S. Kurtz, Report NREL/CP-520-33557, 2003.
- ⁴⁰A. Kosa, L. Stuchlikova, L. Harmatha, J. Kovac, B. Sciana, W. Dawidowski, and M. Tlaczala, *Adv. Electr. Electron. Eng.* **15**, 114 (2017).
- ⁴¹B. Bouzazi, N. Kojima, Y. Ohshita, and M. Yamaguchi, *J. Alloys Compd.* **552**, 469 (2013).
- ⁴²D. J. Friedman, A. J. Ptak, S. R. Kurtz, and J. F. Geisz, in *Proceedings of the 31st IEEE PVSC* (2005), p. 691–694.
- ⁴³P. Omling, L. Samuelson, and H. G. Grimmeiss, *J. Appl. Phys.* **54**, 5117 (1983).
- ⁴⁴J. W. Matthews and A. E. Blakeslee, *J. Cryst. Growth* **27**, 118 (1974).
- ⁴⁵A. E. Zhukov, A. Y. Egorov, V. M. Ustinov, A. F. Tsatsulnikov, M. V. Maksimov, N. N. Faleev, and P. S. Kopev, *Semiconductors* **31**, 15 (1997).